Nuclear Magnetic Resonance Studies of an N^2-Guanine Adduct Derived from the Tumorigen Dibenzo[*a,l*]pyrene in DNA: Impact of Adduct Stereochemistry, Size, and Local DNA Sequence on Solution Conformations

Fabián A. Rodríguez,[†] Zhi Liu,[†] Chin H. Lin,[†] Shuang Ding,[‡] Yuqin Cai,[‡] Alexander Kolbanovskiy,[†] Marina Kolbanovskiy,[†] Shantu Amin,[§] Suse Broyde,[‡] and Nicholas E. Geacintov*[,†]

[†]Department of Chemistry, New York University, New York, New York 10003, United States
[‡]Department of Biology, New York University, New York, New York 10003, United States
[§]Department of Pharmacology, Penn State College of Medicine, Hershey, Pennsylvania 17033, United States

S Supporting Information

ABSTRACT: The dimensions and arrangements of aromatic rings (topology) in adducts derived from the reactions of polycyclic aromatic hydrocarbon (PAH) diol epoxide metabolites with DNA influence the distortions and stabilities of double-stranded DNA, and hence their recognition and processing by the human nucleotide excision repair (NER) system. Dibenzo[*a,l*]pyrene (DB[*a,l*]P) is a highly tumorigenic six-ring PAH, which contains a nonplanar and aromatic fjord region that is absent in the structurally related bay region five-ring PAH benzo[*a*]pyrene (B[*a*]P). The PAH diol epoxide−DNA adducts formed include the stereoisomeric 14S and 14R *trans-anti*-DB[*a,l*]P-N^2-dG and the stereochemically analogous 10S- and 10R-B[*a*]P-N^2-dG (B[*a*]P-dG) guanine adducts. However, nuclear magnetic resonance (NMR) solution studies of the 14S-DB[*a,l*]P-N^2-dG adduct in DNA have not yet been presented. Here we have investigated the 14S-DB[*a,l*]P-N^2-dG adduct in two different sequence contexts using NMR methods with distance-restrained molecular dynamics simulations. In duplexes with dC opposite the adduct deleted, a well-resolved base-displaced intercalative adduct conformation can be observed. In full duplexes, in contrast to the intercalated 14R stereoisomeric adduct, the bulky DB[*a,l*]P residue in the 14S adduct is positioned in a greatly widened and distorted minor groove, with significant disruptions and distortions of base pairing at the lesion site and two 5′-side adjacent base pairs. These unique structural features are significantly different from those of the stereochemically analogous but smaller B[*a*]P-dG adduct. The greater size and different topology of the DB[*a,l*]P aromatic ring system lead to greater structurally destabilizing DNA distortions that are partially compensated by stabilizing DB[*a,l*]P-DNA van der Waals interactions, whose combined effects impact the NER response to the adduct. These structural results broaden our understanding of the structure−function relationship in NER.
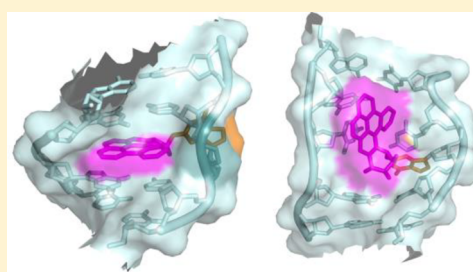
Polycyclic aromatic hydrocarbons (PAHs) are byproducts of fossil fuel combustion and are therefore ubiquitous environmental contaminants in airborne particulates[1] and cigarette smoke.[2] In mammalian cells, PAH compounds are metabolically activated to reactive intermediates by several different pathways that can cause DNA damage and the formation of unstable[3] and stable[4−6] DNA adducts. The widely studied cytochrome P450 pathway generates mutagenic and tumorigenic PAH diol epoxide derivatives[7,8] that react with the exocyclic amino groups of guanine and adenine in DNA to form various stereoisomeric DNA adducts.[5,9] Such DNA adducts have been found in PAH-treated or PAH diol epoxide-treated eukaryotic cells.[10−16]

The carcinogenic activities of PAH compounds and their diol epoxide metabolites depend on the number of aromatic rings and their topological arrangements.[1,17−20] A striking example of such differences in structure−activity relationships is the tumorigenic activity of the fjord region six-ring PAH dibenzo-[*a,l*]pyrene (DB[*a,l*]P) that is ~100-fold[19] greater than the activity of the bay region five-ring benzo[*a*]pyrene (B[*a*]-P).[16−18,21−23] There is significant evidence that adducts derived from the reactions with DNA of dibenzo[*a,l*]pyrene-11,12-dihydrodiol-13,14-epoxide (DB[*a,l*]PDE), the ultimate carcinogenic metabolite of DB[*a,l*]P, are persistent in human[12,14] and mouse[24,25] cells. Indeed, several of the stereoisomeric 14S and 14R DNA adducts derived from the binding of (−)-*anti*-DB[*a,l*]PDE to N^6-adenine are resistant to nucleotide excision repair (NER) in human cell extracts,[26,27] while the 14S-DB[*a,l*]P-dG adduct is modestly repaired. In contrast to the DB[*a,l*]P-derived DNA adducts, the stereoisomeric bay region

guanine B[a]P-N^2-dG and adenine B[a]P-N^6-dA adducts with R and S stereochemistry at the C10 linkage site in double-stranded DNA are more efficiently incised.[26,28] Tumor initiation is a complex, multistage process that includes metabolic activation, the formation of different adducts from a particular PAH adduct, and lesion repair.[19] Moreover, diverse PAHs yield adducts with differing topologies. Dissecting the roles of each of these factors remains an important challenge. A current goal of our research is to discover the contribution made by the different NER efficiencies of the various lesions to the tumorigenic potential of the parent PAH. A basic understanding of these NER differences requires insights into the structural features of these DNA adducts and their relationships to biological function.

The objectives of this work were to compare the effects of the aromatic ring system size and topology on the structural features of the 14S-DB[a,l]P-dG adduct and the previously established structures of the stereochemically analogous 10S-B[a]P-dG[29,30] and 1S-B[c]Ph-dG[31] adducts, as well as the stereoisomeric 14R-DB[a,l]P-dG adduct[32] (Figure 1A). We thereby further our understanding of the DNA lesion

structure–function relationship in the NER mechanism. However, NMR studies of the 14S-DB[a,l]P-dG adduct have not yet been presented. Therefore, the focus of this study was to establish the conformational properties of this adduct in a fully complementary 11-mer DNA duplex and in a "deletion" (Del) duplex that lacks a single nucleotide opposite the lesion (Figure 1B) using NMR and molecular modeling approaches. The conformations of the full duplexes are important for understanding their recognition by cellular DNA repair systems, while the structures of the Del duplexes yield important further insights into the effect of base sequence context on bulky PAH carcinogen–DNA interactions.

■ METHODS

Synthesis and Purification of the 14S-DB[a,l]P-dG Oligonucleotide Adducts. *Caution: DB[a,l]PDE is highly tumorigenic and must be handled with the utmost care to prevent contact with the skin, contamination of laboratory benches, or laboratory items.*

Racemic mixtures of the *anti*-DB[a,l]PDE isomer were provided by the National Cancer Institute (NCI) Chemical Repository for Chemical Carcinogenesis Research. The DNA oligonucleotides were purchased from Integrated DNA Technologies (IDT) and purified by reversed phase HPLC using a C-18 column with a methanol/phosphate gradient. Their masses were verified by MALDI-TOF mass spectrometry. The 14S-DB[a,l]P-dG adduct was synthesized, using previously described methods,[33] in the 5′-CCATCGCTACC-3′ sequence, which has been well studied by our group for different PAH-derived guanine adducts (e.g., refs 29, 31, 32, and 34) and was selected to facilitate structural and functional comparisons. Briefly, ∼3 mg of (±)-*anti*-DB[a,l]PDE was dissolved in 350 μL of THF and added to an 8 mg buffer solution of 5′-CCATCGCTACC-3′ [25 mM sodium acetate, 25 mM Tris, and 25 mM TEAA (pH 11)]. An additional 350 μL of a THF solution was added to this solution, which was then stirred in the dark at room temperature for 8 days, during which the diol epoxides are stable at pH 11, because their acid-catalyzed hydrolysis is suppressed in this highly alkaline environment. The reaction was stopped by adding 3.5 mL of a 1:1 ethyl acetate/ethyl ether mixture, and the organic phase was extracted to remove DB[a,l]P. The solution was then centrifuged to remove solid residues, and all glassware was decontaminated by being rinsed with dilute acid solutions. The products of the synthesis were purified using multiple reversed phase HPLC steps as described previously.[33] Briefly, the modified oliognucleotides were separated from unreacted oligonucleotides using a PRP-1 column with a 5 to 50% acetonitrile/50 mM TEAA buffer gradient in 60 min. The modified stereoisomeric oligonucleotides were then further separated using a 10 to 25% acetonitrile/50 mM TEAA buffer solution in 60 min. The masses of the modified oligonucleotides were determined by MALDI-TOF mass spectrometry methods that verified that the oligonucleotides contained a single modified nucleotide residue. The absolute configuration of the 14S-DB[a,l]P-dG (G*) adduct was determined by digesting the modified 5′-CCATCG*CTACC to the nucleoside level dG* and verifying its stereochemical properties by circular dichroism methods.[35]

The duplexes that were used in these experiments were generated by annealing the purified PAH-modified 11-mer sequence with the complementary unmodified strand using standard methods of mixing the two strands in 1:1 proportions,

A

14S-DB[a,l]P-dG

10S-B[a]P-dG

14R-DB[a,l]P-dG

1S-B[c]Ph-dG
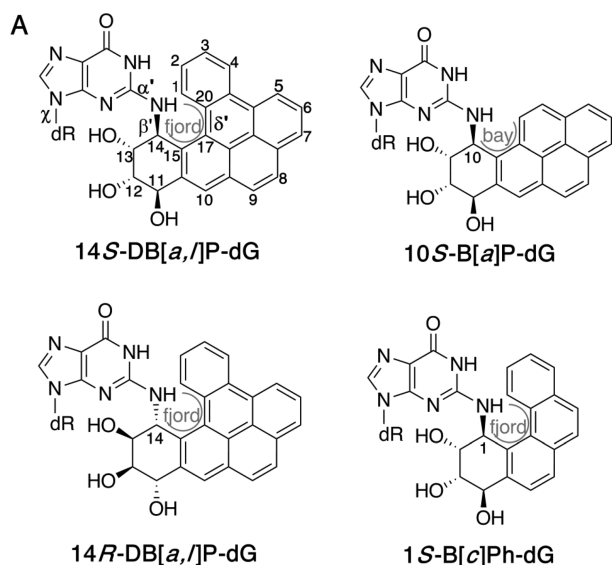
B

Full duplex
5' - C1 - C2 - A3 - T4 - C5 - G6*- C7 - T8 - A9 -C10 -C11-3'
3'- G22-G21-T20-A19-G18-C17-G16-A15-T14-G13-G12-5'

Deletion duplex
5' - C1 - C2 - A3 - T4 - C5 - G6*- C7 - T8 - A9 -C10 -C11-3'
3'- G22-G21-T20-A19-G18   ---   G16-A15-T14-G13-G12-5'

Figure 1. (A) Chemical structures of the 14S-DB[a,l]P-dG, 10S-B[a]P-dG, and 1S-B[c]Ph-dG adducts. The torsion angles α′ (N1−C2−N2−C14), β′ (C2−N2−C14−C13), and δ′ (C15−C17−C20−C1) for the 14S-DB[a,l]P-dG adduct are indicated. The 14S-DB[a,l]P-dG adducts are derived from the *trans* addition reaction of (−)-dibenzo[a,l]pyrene-11R,12S-dihydrodiol 13S,14R-epoxide [(−)-*anti*-DB[a,l]PDE] with N^2-dG, while the 14R stereoisomeric adduct is derived from a similar *trans* addition reaction with the (+)-*anti*-14S,13R,12R,11S enantiomer.[35] The 10S-B[a]P-dG and 1S-B[c]Ph-dG adducts are generated by similar *trans* addition reactions with the stereochemically analogous (+)-7R,8S,9S,10R and (−)-1S,2R,3R,4S diol epoxide enantiomers derived from benzo[a]pyrene (B[a]P) and benzo[c]phenanthrene (B[c]Ph), respectively.[57] (B) Sequences investigated.

then heating the solutions at 90 °C for 2 min, and then allowing for slow cooling and annealing of the two strands.

NMR Measurements. *14S-DB[a,l]P-dG Deletion Duplex.* The two-dimensional nuclear Overhauser effect spectroscopy (NOESY) spectra for the 14S-DB[a,l]P-dG deletion duplex adduct (Figure 1B) in a D_2O phosphate buffer solution at 20 and 15 °C were recorded with mixing times of 40, 70, 120, 200, 250, and 300 ms utilizing a Bruker Avance 500 MHz spectrometer at the Shared Instrumentation Facility (SIF) at New York University. The NOESY spectra in a 90% H_2O/10% D_2O buffer solution with mixing times of 100 and 200 ms at 15 °C (or 150 ms at 4 °C) to visualize the imino proton spectra were recorded with the same Bruker Avance 500 MHz NMR spectrometer. All NOESY data sets were acquired using phase sensitive pulse sequences recorded with the States−TPPI method. The relaxation delay was set to 1.85 s with 512 FIDs, and each FID was recorded with 104 transient scans with 2K complex data points and a spectral width of 10.5 ppm in both dimensions for the spectra in D_2O. The spectral width was 21 ppm for the corresponding spectra in H_2O. The data sets were processed with the standard Bruker processing software package (TOPSPIN version 1.3). Peak assignments were made using SPARKY.[36] Correlation spectroscopy (COSY) and total correlation spectroscopy (TOCSY) methods with mixing times of 80 ms in a D_2O buffer solution at 15 and 20 °C were used for the assignment of the critical cytosine H5−H6 and DB[a,l]P aromatic ring protons in the adduct duplex. The acquisition of the TOCSY and COSY spectra was the same as that for the NOESY spectra. The NMR buffer solution consisted of 10 mM Na_2HPO_4 and 100 mM NaCl (pH 6.8), and 25 nM DSS (2,2-dimethyl-2-silapentane-5-sulfonate, sodium salt) was used as a 0 ppm reference marker.

14S-DB[a,l]P-dG Full Duplex. The two-dimensional NOESY spectra of 14S-DB[a,l]P-dG in the full duplex (Figure 1B) in a D_2O phosphate buffer solution at 11 °C were recorded with mixing times of 50, 100, 200, and 250 ms, at temperatures of 5, 25, and 35 °C. The spectra were recorded utilizing a Bruker Avance 600 MHz spectrometer equipped with a cryoprobe at the New York Structural Biology Center (NYSBC). The NOESY spectra in a 90% H_2O/10% D_2O buffer solution with mixing times of 175 and 250 ms at 15 °C, or 125 and 150 ms at 4 °C to visualize the imino protons, were recorded with the Bruker Avance 500 MHz NMR spectrometer at New York University. The conditions for NOESY spectra and data processing were the same in the full and deletion duplexes, and the relaxation delays were set to 1.5 s in D_2O (1.2 s in H_2O). TOCSY methods with mixing times of 60 ms in a D_2O buffer solution at 5, 11, 15, 25, and 35 °C were used for the assignment of the critical cytosine H5−H6 and DB[a,l]P aromatic ring protons in the adducted duplex. Data acquisition for the TOCSY spectra was the same as for the NOESY spectra.

MD Simulations: Initial Models. *14S-DB[a,l]P-dG Nucleoside.* The initial model for the 14S-DB[a,l]P-dG adduct on the nucleoside level was built from the high-resolution NMR solution structure of the fjord region analogue 1S-B[c]Ph-dG[31] (Figure 1A) with the same stereochemistry at the linkage site and positioned in the identical sequence context. Molecular modeling was employed to extract the modified nucleoside from the 11-mer duplex that was capped with hydrogen atoms at positions O3′ and O5′. We then added two aromatic rings to the B[c]Ph residue to create the initial model of the 14S-DB[a,l]P adduct. This model was subjected to geometry optimization utilizing Gaussian 03[37] at the B3LYP/6-31G* level.

14S-DB[a,l]P-dG Deletion Duplex. The initial model of the adduct in the deletion duplex adopted here was based on the previously established structure of the 10S-B[a]P-dG·Del 11/10-mer adduct duplex[30] to provide a DNA deletion duplex structure. However, the B[a]P moiety in the latter structure was excised and replaced with the DB[a,l]P residue structure that was obtained through QM geometry optimization as described above, and minor steric clashes due to close contacts were alleviated with molecular modeling. This approach yielded an intercalation conformation as a starting model that is consistent with the NMR data (see Results).

14S-DB[a,l]P-dG Full Duplex. The initial model was based on the NMR solution structure of the stereochemically analogous 10S-B[a]P-dG adduct[29] positioned in the minor groove in the identical sequence context, replacing the B[a]P moiety with the DB[a,l]P residue as described above for the deletion duplex. This model was adopted because the NMR data suggest that the DB[a,l]P residue in the 14S-DB[a,l]P-dG full duplex is positioned in the minor groove (see Results). Minor close contacts were alleviated by molecular modeling. Visualization and model building were performed with INSIGHT II (Accelrys Software, Inc.). PyMOL (Schrödinger, LLC) was employed to make molecular images and movies.

MD Protocols. The protocol we utilized to obtain the NMR distance-refined structures entailed unrestrained MD simulations for 3 ns for the initial models, followed by distance-restrained MD simulation for 1 ns. MD simulations were conducted using the AMBER 9 package,[38] and the Cornell et al. force field[39] with the parm99.dat parameter set.[40] The partial charges of the modified nucleoside were computed utilizing quantum mechanical Hartree−Fock calculations with the 6-31G* basis set employing the Gaussian 03 package.[37] The charges were then fit to each atomic center with the RESP algorithm.[39,41] Other force field parameters used for the 14S-DB[a,l]P-dG adduct were assigned to be consistent with the rest of the AMBER force field. Tables S1 and S2 (Supporting Information) list these force field parameters. The details of the MD simulation protocol are provided in the Supporting Information. For the 14S-DB[a,l]P-dG deletion duplex, five representative structures were extracted from the restrained MD simulation using the PTRAJ module of AMBER 9[38] and used for analyses. For the full duplex, one minor groove structure that best represented the NMR data based on the intermolecular NOEs was selected to describe the structural features of this adduct. The sixth-root R factor (R_x) was calculated by CORMA[42] to evaluate the best representative structure derived from the restrained MD simulation

■ RESULTS

NMR Characterization of the 14S-DB[a,l]P-dG·Del Duplex. *Exchangeable Proton Spectra.* The one-dimensional (1D) exchangeable proton spectrum (10.5−13.8 ppm) of the 14S-DB[a,l]P-dG·Del 11/10-mer duplex in H_2O buffer (pH 6.8) at 15 °C is shown in Figure 2A. The imino proton assignments are based on the analysis of the NOE imino− imino proton cross-peaks, and cross-peaks between imino protons and other nearby protons in the Watson−Crick partner flanking base pairs.[43,44] We observed eight well-resolved imino proton resonances, including two upfield-shifted imino proton resonances at 11.16 and 10.72 ppm. The two terminal imino protons, G22 and G12, could not be clearly identified because
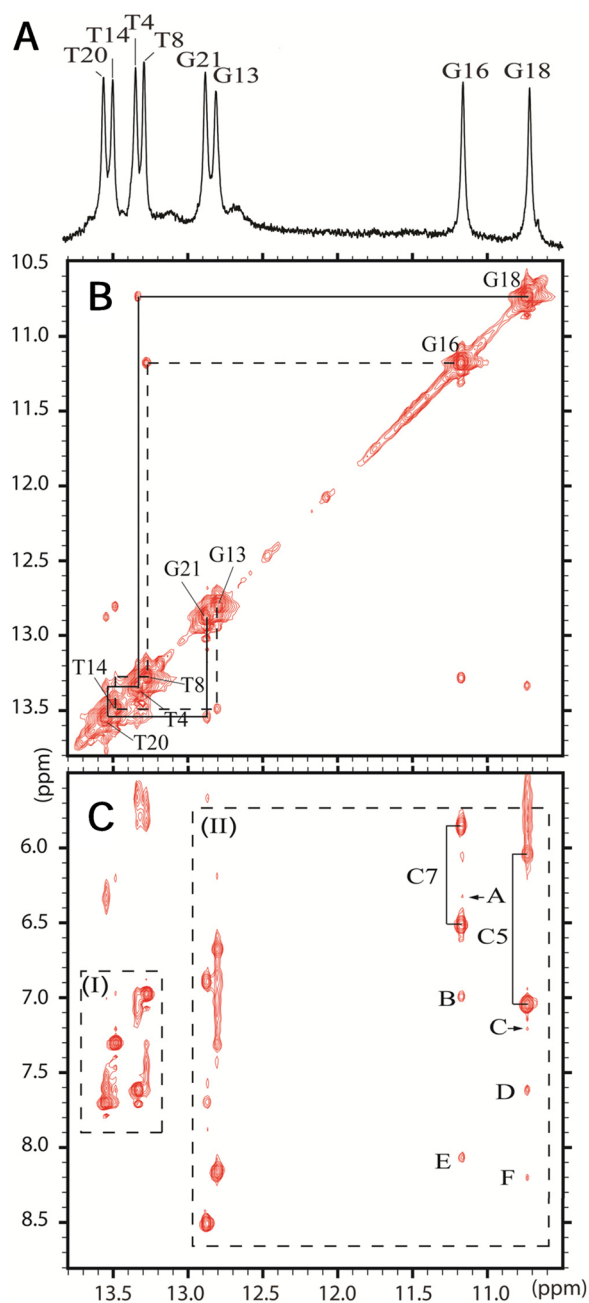
Figure 2. 11/10-mer deletion duplex. (A) One-dimensional imino proton spectrum of the 14*S*-DB[*a,l*]P-dG·Del adduct in H$_2$O recorded at 15 °C in a 500 MHz spectrometer in a buffer solution (pH 6.8) (10.5−13.8 ppm). (B) Portion of a 2D NOESY (200 ms mixing time, 15 °C) contour plot spectrum focused on the symmetric imino-to-imino (10.5−13.8 ppm) region. The sequential assignment is traced starting at G21 to G18 and from G16 to G13. No imino-to-imino NOE cross-peak is observed between G16 and G18. (C) Portion of a 2D NOESY (200 ms mixing time, 15 °C) contour plot focused on the imino (10.5−13.8 ppm) to amino/base (5.5−8.8 ppm) proton region. Box I shows the characteristic Watson−Crick hydrogen-bonded thymine imino−adenine H2 proton resonances. Box II shows the characteristic Watson−Crick hydrogen-bonded guanine imino−cytosine amino proton NOEs. In particular, NOE connectivities between the imino proton of G16 and G18 and their complementary base amino groups are shown. Labels A−F in panel C are as follows: (A) DB[*a,l*]P(H14)−16(NH1), (B) DB[*a,l*]P(H3)−18(NH1), (C) 15(H2)−16(NH1), (D) 19(H2)−18(H1), (E) DB[*a,l*]P(H5)−16-(NH1), and (F) DB[*a,l*]P(H4)−18(NH1).

of terminal fraying at 15 °C. The unpaired G6*(NH1) proton could not be identified either, thus indicating fraying and fast exchange with the solvent. The sharp imino proton resonances are characteristic of a well-defined single conformer.

Figure 2B depicts a portion of a NOESY (200 ms mixing time) contour plot at 15 °C in the symmetrical 10.5−13.8 ppm region. The imino−imino proton sequential assignments are shown by solid lines for the central 8 bp starting from T20 to G13. The sequential assignments can be traced without interruption from G21 to G18 and from G16 to G13. The terminal G12 and G22 are not discernible because of terminal end fraying effects. The absence of the connectivities between G6*(NH1) and G16(NH1) or G18(NH1) imino protons indicates that these guanine residues are not in their normal Watson−Crick conformations. Furthermore, we did not detect any NOEs between G6*(NH1) and its own amino group; these observations suggest that this imino proton is exposed to solvent and that its resonance is broadened because of rapid proton exchange with H$_2$O protons. There is no NOE cross-peak between the G16(NH1) and G18(NH1) imino protons, which indicates that these bases are far apart, which is consistent with the intercalation of the DB[*a,l*]P ring system between these base pairs.

A NOESY (200 ms mixing time) contour plot at 15 °C in H$_2$O buffer is shown in Figure 2C within the imino (10.5−13.8 ppm) and amino/base H2 (5.5−8.8 ppm) NOE cross-peak region that is characteristic of well-defined Watson−Crick base pairing. NOE cross-peaks are evident between the narrow, upfield-shifted imino proton of dG16 (11.16 ppm) flanking the lesion site and the two amino protons of dC7 (6.51 and 5.85 ppm). Likewise, the similarly narrow and upfield-shifted dG18 (10.72 ppm) imino proton flanking the lesion on the other side exhibits cross-peaks with the 6.04 and 7.04 ppm amino protons of dC5 (Figure 2C, box II). These results establish Watson−Crick base pair formation at the two base pairs flanking the lesion site. Similarly, the thymine imino proton−H2 adenine cross-peaks establish that Watson−Crick base pairing is maintained at all A-T base pairs (Figure 2C, box I). The large upfield shifts (>1 ppm) observed for the G16(NH1) and G18(NH1) protons are attributed to ring current shielding effects originating from the intercalation of the DB[*a,l*]P moiety that is inserted between these two adjacent base pairs (see below). The chemical shifts of ^{1}H nuclei in aromatic molecules are dramatically shifted because of such aromatic ring current effects.[45]

Nonexchangeable Proton Spectra. An expanded NOESY spectrum (300 ms mixing time) in D$_2$O buffer at 20 °C, focused on the base (purine H8 and pyrimidine H6) proton (6.45−8.45 ppm) and sugar H1′ or cytosine H5 proton (4.9−6.8 ppm) region, is depicted in Figure 3. The well-resolved DNA base and sugar protons were identified by analysis of through-space (NOESY) connectivities and through-bond correlations in COSY and TOCSY spectra at the same temperature. Sequential assignments between base protons and their own and 5′-flanking sugar H1′ protons can be traced on the modified strand for the A3-T4-C5-G6*-C7-T8-A9 segment (solid lines), except at the C5(H1′)−G6*(H8) step indicated by an empty square (ñ). For the unmodified strand, the sequential assignment can be traced for the entire strand with only the disruption at the G16-G18 step. The assignments are shown by the dashed lines in the case of the T14-G16 and G18-A19-T20 segments. Weak cross-peaks are observed in the case of the T4(H1′)−C5(H6) and T4(H6)−C5(H6) (labeled
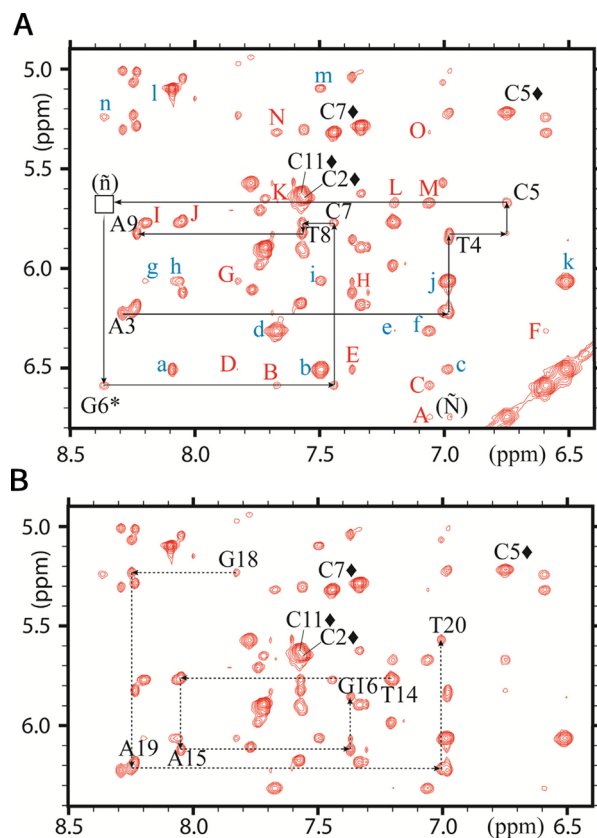
A

B

Figure 3. 11/10-mer deletion duplex. Expanded contour plot of a NOESY spectrum (300 ms mixing time) recorded at 20 °C in a D_2O buffer solution. The connectivities between the base (purine H8 and pyrimidine H6) protons (6.45−8.45 ppm) and the sugar H1′ or cytosine H5 protons (4.9−6.8 ppm) are traced. The NOE connectivities between the base proton and its own and 5′-flanking sugar H1′ protons from dA3 to dA9 on the modified strand are shown as solid lines in panel A, while those from dT14 to dG16 and from dG18 to T20 on the unmodified strand are shown as dashed lines in panel B. The cytosine H5−H6 connectivities are indicated by bullets. The red uppercase letters indicate intermolecular NOE connectivities between DNA and carcinogen protons, while the blue lowercase letters indicate intramolecular carcinogen connectivities. On the modified strand, there is a break in the sequential assignment at the C5(H1′)−G6*(H8) cross-peak that is indicated by (ñ) and results from the displacement to the major groove of G6*, as well as on the nonmodified strand from G16(H1′) to G18(H1′) due to the deletion of the C17 base with intercalation of the DB[a,l]P rings between G16 and G18. Note the unusual large upfield chemical shift of H6 of dC5 to 6.75 ppm and the downfield chemical shift of G6*(H8) to 8.36 ppm (Table S3 of the Supporting Information). The cross-peak labeled (ñ) is the C5(H1′)−G6*(H8) cross-peak and that labeled (Ñ) the C5(H6)−T4(H6) cross-peak. The carcinogen−carcinogen cross-peaks labeled in blue lowercase letters are as follows: (a) DB[a,l]P-(H8−H10), (b) DB[a,l]P(H8−H9), (c) DB[a,l]P(H8−H6), (d) DB[a,l]P(H14−H1), (e) DB[a,l]P(H14−H3), (f) DB[a,l]P(H8−H2), (g) DB[a,l]P(H7−H4), (h) DB[a,l]P(H7−H5), (i) DB[a,l]P-(H7−H9), (j) DB[a,l]P(H7−H6), (k) DB[a,l]P(H7−H8), (l) DB[a,l]P(H11−H10), and (m) DB[a,l]P(H11−H9). The carcinogen−DNA cross-peaks labeled in red uppercase letters are as follows: (A) C5(H6)−DB[a,l]P(H2), (B) G6*(H1′)−DB[a,l]P(H1), (C) G6*(H1′)−DB[a,l]P(H2), (D) DB[a,l]P(H8)−G18(H8), (E) DB-[a,l]P(H8)−G16(H8), (F) DB[a,l]P(H14)−G6*(H1′), (G) DB[a,l]-P(H7)−G18(H8), (H) DB[a,l]P(H7)−G16(H8), (I) C7(H1′)−DB[a,l]P(H4), (J) C7(H1′)−DB[a,l]P(H5), (K) C5(H1′)−DB[a,l]-P(H1), (L) C5(H1′)−DB[a,l]P(H3), (M) C5(H1′)−DB[a,l]P(H2), (N) C7(H5)−DB[a,l]P(H1), and (O) C7(H5)−DB[a,l]P(H3).

Ñ) connectivities. The NOE connectivity between the adducted guanine G6* and its 5′-flanking base C5 is missing entirely (ñ). The connectivities are also perturbed at the (DB[a,l]P)dG6-dC7 step because the NOEs between H2′ and H2″ of dG6* and H6 of dC7 are very weak (Figure S1 of the Supporting Information). However, a weak but well-defined G6*(H1′)−C7(H6) cross-peak is discernible (Figure S2 of the Supporting Information), although NOEs between the C5(H6)−G6*(H8) and G6*(H8)−C7(H6) protons are missing. We detected strong NOEs between either the H5 or H6 proton of dC7 and either the sugar H1′ or H4′ proton of dG6* in the 40 ms mixing time NOESY spectrum (examples shown in Figure S2 of the Supporting Information). These results suggest that the H5 and H6 protons of C7 that protrude into the major groove are close to the H1′ and H4′ protons of the G6* sugar residue, as discussed previously.[30] The results derived above, together with the analysis of the NOESY spectrum in water, indicate that the adducted deoxyguanosine is displaced into the major groove with the DB[a,l]P aromatic ring system intercalated between the C5:G18 and C7:G16 base pairs.

The sugar puckering and glycosidic bond conformation at the lesion site were probed using relative intensities in a NOESY spectrum with a 40 ms mixing time. The glycosidic torsion angle χ is in the normal *anti* conformation, which is manifested by a weak G6*(H8)−G6*(H1′) NOE cross-peak.[43] The NOE cross-peak between the base G6*(H8) and sugar G6*(H3′) proton is also weak, indicative of a sugar conformation in the overall southern/C2′-*endo* domain of the pseudorotation cycle.[44]

Chemical Shift Perturbations. The chemical shifts exhibited by the nonexchangeable protons in the 14S-DB[a,l]P-dG·Del 11/10-mer duplex relative to the same protons in an unmodified duplex are depicted in Figure 4A. Compared with the corresponding proton chemical shifts in the unmodified duplex, significant upfield shifts for the base H5 and sugar (H2′ and H2″) protons of dC5 are noted, while the base H8 and sugar (H1′, H2′, H3′, and H4′) protons of dG6* are all downfield-shifted. The H8 base protons of both G16 and G18 are upfield-shifted (Figure 4A). These results are consistent with ring current effects that arise from the intercalated polycyclic aromatic ring system with the modified dG6* base being displaced from the DNA helix. Analogous effects were observed in the case of the stereochemically similar 10S-B[a]P-dG 11/10-mer deletion duplex.[30]

The nonexchangeable polycyclic aromatic DB[a,l]P residue protons were assigned by analysis of through-bond TOCSY (an example is shown in Figure S3 of the Supporting Information) and through-space NOESY connectivities. Some of the intramolecular NOEs between protons of the polycyclic aromatic ring system are shown in Figure 3A (connectivities a−m). The chemical shifts of the aliphatic and aromatic DB[a,l]P ring protons are listed in Table 1, and examples are shown graphically in Figure S5 of the Supporting Information. Almost all of the DB[a,l]P residue aromatic protons are upfield-shifted from their normal values of 8.0−8.5 ppm, which is consistent with ring current effects due to the aromatic G16 and/or G18. With the exception of the H4 and H5 protons of DB[a,l]P, these upfield shifts are similar to those observed in the case of the polycyclic aromatic ring protons of the 10S-B[a]P-dG 11/10-mer deletion duplex that are uniformly upfield-shifted.[30] These observations also support the intercalated conformation of the DB[a,l]P ring system.

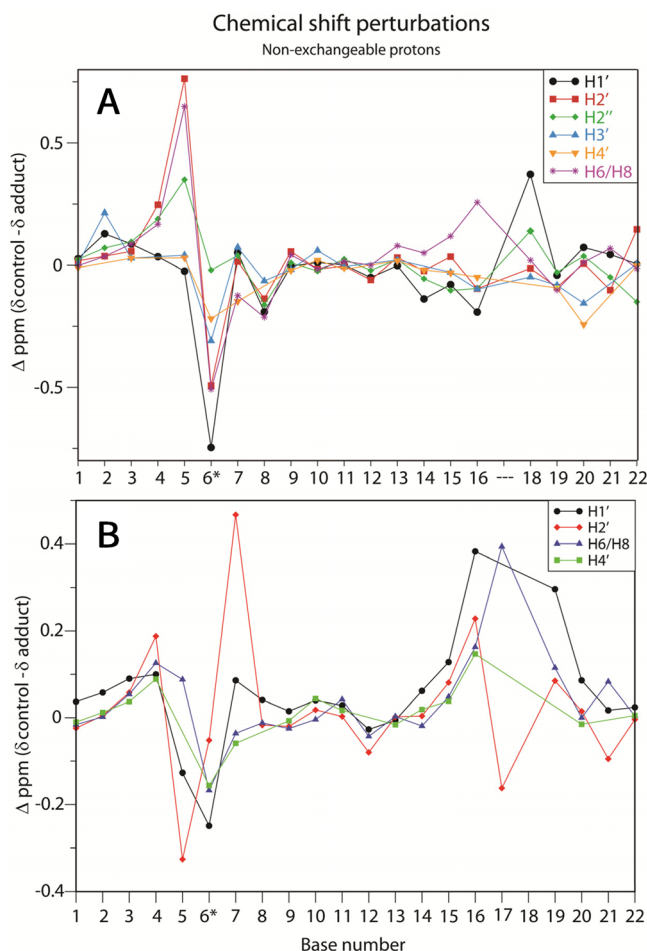## Chemical shift perturbations
Non-exchangeable protons

Figure 4. Chemical shift values relative to unmodified control duplexes. (A) 11/10-mer deletion duplex. Chemical shift perturbations of the nonexchangeable DNA base/sugar protons relative to the unmodified control 11-mer duplex. The positive values of Δ ppm (δ control − δ adduct) are upfield chemical shift resonances, while negative values are downfield chemical shift proton resonances. (B) 11/11-mer full duplex. Graphical representation of the chemical shift perturbations of nonexchangeable DNA protons relative to the unmodified control 11-mer duplex. While the points are not mathematically related, we connect them only to facilitate comparisons.

Intermolecular NOEs. A total of 55 intermolecular NOEs between the nonexchangeable aromatic DB[a,l]P and nearby exchangeable and nonexchangeable base and sugar protons were identified and assigned (some are shown in Figure 3A) and summarized in Table 1. The DB[a,l]P H1, H2, H3, and H4 protons exhibit NOEs predominantly with C5 and C7 base and sugar protons. These NOEs indicate that the 1−2−3 edge of the aromatic ring in the fjord region is close to the modified strand. Furthermore, the DB[a,l]P H14 proton exhibits NOEs with 3′-base pair C7:G16 base protons, and there are no NOEs between H10, H11, H12, and H13 DB[a,l]P protons and DNA residues (Table 1). Thus, the benzylic ring of DB[a,l]P appears to be positioned in the spacious major groove, directed toward the 3′-side of the modified strand.

NMR-Restrained MD Simulation Structure: Intercalative Conformation. NMR distance-restrained MD simulations were employed to define the solution structure of the 14S-DB[a,l]P-dG deletion duplex. The initial model was based on the B-DNA NMR solution structure of the stereochemically

identical intercalated 10S-B[a]P-dG deletion duplex,[30] as described in Methods. Restrained MD simulations were conducted with explicit solvent and counterions, as detailed in Methods and the Supporting Information. Five representative structures (Figure S4 of the Supporting Information) were selected from the restrained MD simulation using the *PTRAJ* module of AMBER. The best representative structure from *PTRAJ* is shown in panels A and B of Figure 5. The sixth-root R factor (R_x) was calculated by CORMA[42] to evaluate the best representative structure from the restrained MD simulation (Table 2).

As shown in panels A and B of Figure 5, in the 14S-DB[a,l]P-dG deletion duplex structure, the DB[a,l]P aromatic ring system is intercalated between the C5:G18 and C7:G16 flanking base pairs, with the benzylic ring of the adduct positioned in the major groove. This intercalation model is supported by the experimentally observed upfield shifts of the aromatic DB[a,l]P protons, especially the H6, H7, H8, and H9 protons that are significantly upfield shifted (Figure S5 of the Supporting Information), and the close contact of this group of protons with the H8 base and sugar protons of G16 and G18. As mentioned earlier, these upfield shifts are attributed to ring current effects due to stacking of G16 and G18 with the DB[a,l]P ring system and are consistent with the intercalation of the 6−7−8−9 edge (Figure 1A) of the carcinogen aromatic ring system between G16 and G18.

The modified unpartnered guanine G6*, linked to the DB[a,l]P ring system, is displaced into the major groove. In the model, one face of G6* is exposed to the solvent. The displacement of G6* with solvent exposure is consistent with the absence of the G6* imino proton resonance in the 1D exchangeable proton spectrum, and the absence of NOE cross-peaks between the G6* imino proton and its own amino with imino protons of flanking bases. The major groove positioning of the G6* residue is also supported by NOEs between C7(H6) and G6*(H4′) and between C7(H5) and G6*(H1′) at a 40 ms NOE mixing time (Figure S2 of the Supporting Information), because H6 and H5 of C7 are positioned in the major groove. The base major groove edge and sugar ring of dC5 are stacked over the displaced guanine (Figure 5A,B), as shown by downfield shifts of the dG6* base protons and upfield shifts of dC5 protons and correlated shifts of some of the sugar protons of both nucleotides (Figure 4A and Table S3 of the Supporting Information).

The covalent linkage bond torsion angles α′ and β′ (Figure 1A) and the glycosidic torsion angle χ in our model have average values of 144 ± 4°, 285 ± 3°, and 253 ± 7°, respectively. The glycosidic torsion is in the *anti* domain, as shown by a weak G6*(H8)−G6*(H1′) NOE cross-peak.[46] In the model, the fjord region deviates from planarity with the dihedral angle δ′ (C15−C17−C20−C1) (Figure 1A) having an average value of 16 ± 1°. This twist of the fjord ring optimizes stacking between the DB[a,l]P aromatic rings and the flanking base pairs. The sugar pucker in the distance-refined structure at G6* is C1′-*exo* − C2′-*endo* (pseudorotation parameter P ∼ 125),[47] consistent with the weak NOE between G6*(H8) and G6*(H3′)[44] that is characteristic of the overall C2′-*endo* (southern) conformational region of the pseudorotation cycle.[48]

The base pairs flanking the lesion, C5:G18 and C7:G16, retain Watson−Crick hydrogen bonding, as shown by NOEs between the guanine imino protons and their partner cytosine amino protons. These two pairs stack well with the DB[a,l]P

Table 1. Observed Intermolecular NOEs in the 14S-DB[*a,l*]P-dG·Del 11/10-mer Duplex

DB[*a,l*]P proton	intermolecular NOEs[a]
H1 (7.68 ppm)	C5(H1′), C5(H5), C5(H6), G6*(H1′), C7(H5), G18(H1)
H2 (7.06 ppm)	C5(H1′), C5(H2′), C5(H2″), C5(H4′), C5(H6), G6*(H1′), <u>G6*(H5″)</u>, <u>G6*(H5′)</u>, G6*(H4′), C7(H1′), C7(H5), C7(H6)
H3 (7.20 ppm)	C5(H1′), C5(H2′), C5(H2″), C5(H4′), G6*(H1′), C7(H4′), C7(H5), C7(H6), G18(H1), G6*(H4′), <u>C7(H1′)</u>, <u>G6*(H5′)</u>, <u>G6*(H5″)</u>
H4 (8.20 ppm)	C7(H1′), G16(H1), G18(H1)
H5 (8.06 ppm)	<u>C7(H1′)</u>, G16(H1), G18(H1)
H6 (6.99 ppm)	G16(H8), G18(H8), <u>G16(H1′)</u>
H7 (6.07 ppm)	G16(H1′), G16(H2′), G16(H2″), G16(H8), G18(H8)
H8 (6.51 ppm)	G16(H1′), G16(H2′), G16(H2″), G16(H8), G18(H8)
H9 (7.50 ppm)	G16(H8)
H10 (8.09 ppm)	
H11 (5.10 ppm)	
H12 (4.62 ppm)	
H13 (4.55 ppm)	
H14 (6.32 ppm)	G6*(H1′), C7(H5), C7(H6), G16(H1)

[a]The underlined intermolecular distances were not used for the restrained MD simulations because of the overlap with other cross-peaks. However, the total volumes of the overlapped peaks were used for the R_x calculation as unresolved peaks.

aromatic rings, and the existence of stacking interactions is supported by the unusual upfield shifts of the C5:G18 and C7:G16 base pair imino protons (Figure 2A). The distance between G16(H1′) and G18(H8) averages 7.2 ± 0.2 Å, consistent with the lack of connectivity at the G16-G18 step in the NOESY spectrum (Figure 3B), and reflects the backbone stretch induced by intercalation of the DB[*a,l*]P aromatic ring system. The other base pairs, except for one base pair at each end, retain normal Watson–Crick hydrogen bonding, as supported by NOEs between imino and amino protons (Figure 2C).

NMR Characterization of the 14S-DB[*a,l*]P-dG·dC Full Duplex. *Exchangeable Proton Spectra.* The 1D exchangeable proton spectrum (10.8−13.8 ppm) of the 14S-DB[*a,l*]P-dG 11/11-mer duplex in H_2O buffer (pH 6.8), recorded at 500 MHz and 10 °C, is shown in Figure 6A. The assignments of the imino proton resonances are shown, and the values are summarized in Table S4 of the Supporting Information. The 1D spectrum exhibits two broad and upfield-shifted resonances that are identified as the G18 and G6* imino protons (11.88 and 11.12 ppm, respectively). In contrast to that of G18, the G16 imino proton resonance (12.36 ppm) is relatively sharp. The unusual widths of the G18 and G6* resonances indicate that these imino protons are undergoing rapid exchange with water.[49] Also, the imino proton resonance of T4 is broader than those of other thymines and also exhibits a noticeable shoulder (Figure 6A and Figure S6 of the Supporting Information). The broadness of the T4 imino proton resonance is likely due to a greater than normal solvent exposure, and the shoulder is suggestive of conformational flexibility. By contrast, the G16 imino proton resonance is very sharp, indicating that there is no abnormal solvent exchange. Overall, the severe distortions at the G6*:C17 and C5:G18 base pairs continue more modestly up to the T4:A19 base pair, which is consistent with a 5′-orientation of the bulky DB[*a,l*]P aromatic ring system.

A portion of an NOE contour plot (175 ms mixing time) at 10 °C focused on the symmetrical 10.8−13.8 ppm region is shown in Figure 6B. The sequential imino−imino proton connectivities, or lack thereof, are shown by arrows for the 9 bp starting from G21 and going to G12. The G6* imino proton is identified by a weak cross-peak to the G16(NH1) proton. The positions of missing cross-peaks between T4(NH1) and G18(NH1) and between G18(NH1) and G6*(NH1) are

indicated by empty squares. Increasing the contour plot level does not reveal any cross-peaks in the positions indicated by the squares. These results indicate that the canonical DNA structure is perturbed at the G18 base on the 5′-side of the lesion site and at the adducted base G6*.

Figure 6C shows a portion of an NOE (175 ms mixing time) contour plot at 10 °C in H_2O buffer; characteristic cross-peaks between imino (12.2−13.8 ppm) protons and amino and base H2 (6.2−8.7 ppm) protons of the well-defined Watson−Crick base pairs are observed on the 3′-side of the adduct. In region I, cross-peaks are observed among all four A:T base pairs, but the intensities of the cross-peaks between the T8:A15 and T4:A19 base pairs are weaker then the NOEs between the T14:A9 and T20:A3 base pairs. Both base pairs are more distant from the site of the adduct at G6*, and these results indicate that the structural perturbation due to the adduct extends 1 bp beyond the G16:C7 and G18:C5 base pairs adjacent to the adduct. In box II, cross-peaks labeled A1 and A2 indicate Watson−Crick base pairing between the G16(NH1) and C7(NH1) and C7(NH2) protons, respectively. A weak cross-peak between the G16(NH1) imino and A15(H2) base protons is also observed (A′). By magnifying the contour plot 4-fold (4×), we were able to observe two cross-peaks, between the G16 imino proton and DB[*a,l*]P residue aliphatic protons H13 and H11. A further increase in the contour plot level did not reveal the existence of any additional cross-peaks that could have been attributable to G18:C5 or G6*:C17 Watson−Crick base pairing. Moreover, there is no indication of any cross-peak between DB[*a,l*]P protons and the partially solvent-exposed G18 or G6* imino protons. The other NOEs in region I involve guanines G21 and G13 that are distant from the site of the adduct but are consistent with normal base pairing.

The temperature dependence of the imino proton spectrum is shown in Figure S6 of the Supporting Information. The imino proton assignments shown in the 10 °C spectrum can be easily extrapolated to other temperatures. The behavior of the T4, G18, and G6* imino protons is particularly striking. At 0 °C, the T4 imino proton resonance is relatively sharp, but as the temperature is increased, it broadens and almost vanishes at 35 °C. On the other hand, the G18 and G6* imino proton resonances are not discernible at 0 °C, but they become visible because some narrowing becomes evident at the higher temperatures of 10 and 25 °C; however, they start to disappear
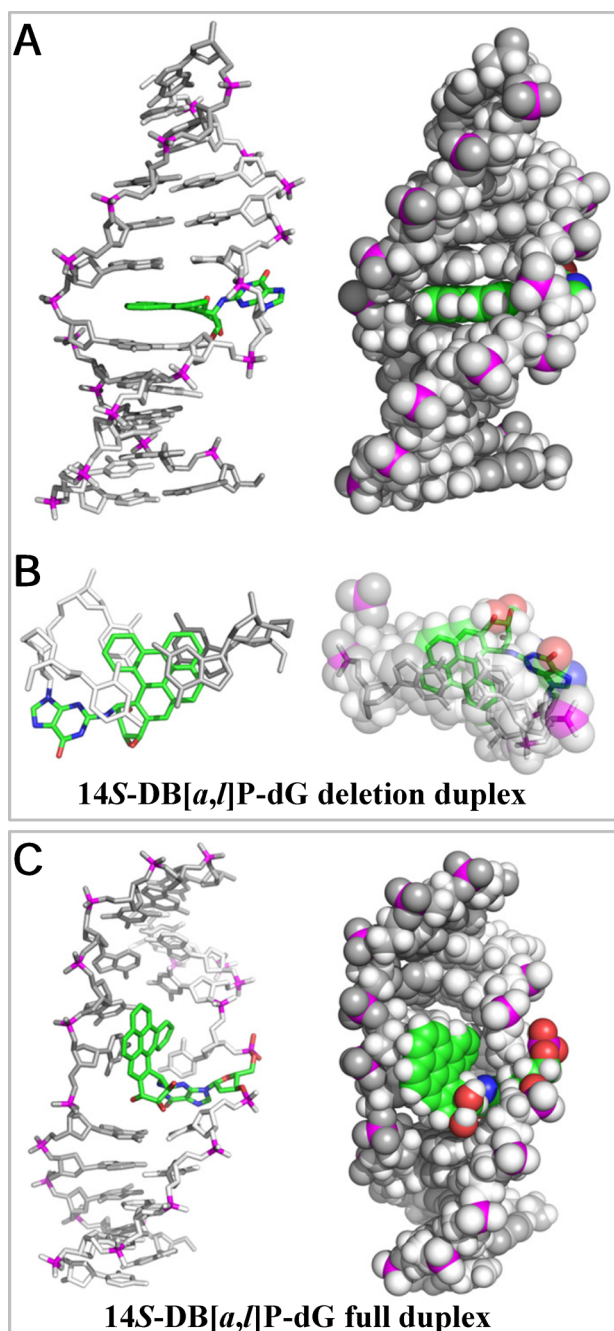
Figure 5. Structural features of 14*S*-DB[*a,l*]P-dG adducts in deletion and full duplexes. (A) 11/10-mer deletion duplex. One 14*S*-DB[*a,l*]P-dG·Del adduct structure was selected from the five structures extracted from the restrained MD simulation that best represents the NMR data. The view is into the minor groove. (B) Stacking pattern of the 14*S*-DB[*a,l*]P-dG·Del adduct in the deletion duplex. The view is looking down the helix axis in the 5′ → 3′ direction. The DB[*a,l*]P rings are intercalated between C5:G18 and C7:G16 base pairs. (C) 11/11-mer full duplex. One structure of the 14*S*-DB[*a,l*]P-dG·dC adduct in the 11-mer full duplex, selected from the restrained MD simulation that represents the NMR data. The view is into the minor groove. The 14*S*-DB[*a,l*]P-dG adduct is colored by atom: green for carbon, red for oxygen, and blue for nitrogen. The phosphorus atoms of the DNA are colored magenta, and the rest of the DNA is colored light gray. The hydrogen atoms in the DNA duplexes are not displayed for the sake of clarity. Structures on the left are rendered as sticks and those on the right in CPK.

Table 2. MD Restraints and Statistical Analysis of the 14*S*-DB[*a,l*]P-dG·Del 11/10-mer Duplex

NMR distance restraints	
total no. of DNA distance restraints	422
exchangeable proton distance restraints	38
nonexchangeable proton distance restraints	342
hydrogen bond restraints	42
total no. of carcinogen distance restraints	29
total no. of intermolecular distance restraints	55
exchangeable distance restraints	7
unresolved peaks	0
nonexchangeable distance restraints	41
unresolved peaks	7
structural statistics	
NOE violations (Å)	0.2
sixth-root R factor (R_x) ($\times 10^{-2}$)	0.0449

as the temperature is increased further to 35 °C. By contrast, the G16(NH1) and other imino proton resonances remain rather sharp throughout the temperature range of 10−35 °C.

These results suggest that at 0 °C the lesion site, especially the G6*:C17 and G18*:C5 base pair imino proton resonances are broadened due to exchange mechanisms and conformational heterogeneity at the lower temperatures (Figure 6C). By contrast, the G16:C7 and T4:A19 base pairs appear to be normal at 0 °C. When the temperature is increased to 25 °C and even 35 °C, the conformational flexibility of the bases in the fluid state indicates some degree of episodic weak hydrogen bonding at the G6*:C17 and G18:C5 base pairs, as manifested by the weak and broadened imino proton resonances that are observed at these temperatures, while hydrogen bonding at the G16:C7 base pair remains sharp and intact (Figure S6 of the Supporting Information). By contrast, while the hydrogen bonding at the T4:A19 base pair is prominent at 10 °C, the T4 imino proton resonance broadens and its intensity diminishes as the temperature is further increased to 25 and 35 °C (Figure S6 of the Supporting Information), indicating diminished Watson−Crick hydrogen bonding and local melting of the duplex at the T4:A19 base pair, as well as at the G18:C5 and G6*:C17 base pairs. In summary, these observations indicate that the adduct distorts the helix on the 5′-side of G6*, that this disturbance extends over 2 bp, and that the DB[*a,l*]P aromatic ring system is therefore positioned on the 5′-side of G6*.

Nonexchangeable Proton Spectra. The expanded NOESY spectrum (200 ms mixing time, 600 MHz) in D₂O buffer at 11 °C focused on the base (6.7−8.4 ppm) and base H5 and sugar H1′ proton (4.35−6.3 ppm) region is depicted in Figure 7. The sequential assignment between base protons to their own and 5′-flanking sugar H1′ protons on the modified strand can be traced within the A3-T4-C5-G6*-C7-T8-A9 segment (solid lines) with a break between G6* and C7 (box ñ, Figure 7, top panel). The A3(H1′)−T4(H6) cross-peak is normal, indicating that T4 is in its proper Watson−Crick position at this temperature (11 °C). The T4(H1′)−C5(H6) cross-peak overlaps with the cross-peak between C5(H1′) and C5(H6); the C5(H1′)−G6*(H8) cross-peak is very weak and can be observed only if the contour diagram is cut lower by a factor of ∼2 (cross-peak A, shown in the bottom panel). The G6*(H1′)−C7(H6) cross-peak is very clearly defined, and its intensity is normal. However, the C7(H1′)−C7(H6) cross-peak overlaps partially with the C5(H1′)−C5(H6) cross-peak,
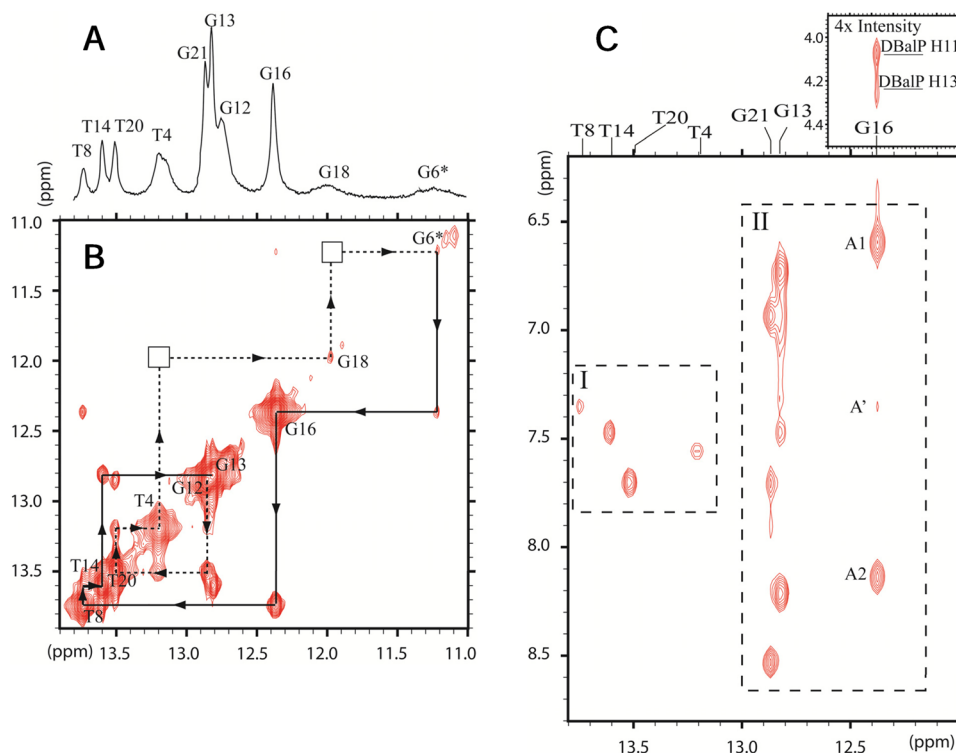
Figure 6. NMR characteristics of 11/11-mer duplexes in H$_2$O. (A) 1D spectrum (10.8−13.8 ppm) of the 14S-DB[a,l]P-dG·dC adduct recorded at 10 °C in a 500 MHz spectrometer in a buffer solution (pH 6.8). (B) 2D symmetric imino−imino proton region (10.8−13.8 ppm) of a NOESY spectrum at a 175 ms mixing time at 10 °C showing the sequential assignment of the five central bases. The sequential assignment is broken at the T4(NH3)−C18(NH1) cross-peak and at the C18(NH1)−G6*(NH1) cross-peak, as indicated by the empty squares. (C) Portion of a 2D NOESY (175 ms mixing time) contour plot recorded at 500 MHz and 10 °C in a water solution showing NOE connectivities between imino (12.0−13.8 ppm) and amino/base (6.2−8.8 ppm) protons. Region I shows characteristic signs of the Watson−Crick hydrogen-bonded thymine imino−adenine H2 proton cross-peak across the duplex. Region II shows characteristic signs of the Watson−Crick hydrogen-bonded guanine imino−cytosine amino proton cross-peak across the two strands. G16(NH1)−C7(NH2) cross-peaks are labeled A, and the G16(NH1)−A15(H2) NOE is labeled A′. At a 4× intensity contour level increment, it is possible to observe two NOE cross-peaks between G16(NH1) and carcinogen protons H13 and H11. There is no evidence of Watson−Crick hydrogen bonding in the case of the putative G6*:C17 and C5:C18 base pairs.

and the C7(H1′)−T8(H6) cross-peak overlaps partially with the T8(H6)−T8(H1′) cross-peak.

In the case of the unmodified strand, the sequential assignment between base protons to their own and 5′-flanking sugar H1′ protons for the T14-A15-G16-C17-G18-A19-T20 segment cannot be followed entirely (dashed lines, Figure 7, top and bottom panels). For example, a normal NOE is observed between A15(H1′) and G16(H8); however, the G16(H8)−G16(H1′) NOE is weak, and a very weak G16(H1′)−C17(H6) NOE can be observed. However, the C17(H6)−(H1′) NOE could not be identified. No other connectivities to C17(H6) are evident, and the NOEs connecting the C17-G18-A19-T20 segment are missing. However, the NOE connectivities can be traced from T20 to the terminal base G22 in the unmodified strand. With a 2-fold increase in the contour level (2× intensity, Figure 7, bottom panel), several cross-peaks labeled A−G become observable. The NOEs labeled C, D, and G are DNA−carcinogen cross-peaks. Peaks A and B are between G6*(H8) and C5 (H1′) and G6*(H1′), respectively. Peak E represents cross-peaks between A19(H1′) and T20(H6). Peak F represents a missing cross-peak between A19(H1′) and A19(H8). The G6* and A19 base protons, which overlap at 11 °C, were distinguishable in the NOESY (250 ms mixing time) spectrum at 25 °C (Figure S7 of the Supporting Information). We estimate the chemical shift value for the A19 base proton through a cross-peak observed

between the methyl group of T20 and the base proton of A19 (Figure S7 of the Supporting Information). Because it was not possible to determine the sequential assignments for the C17-G18-A19-T20 segment of the unmodified strand, the position of the G18(H8) proton resonance could not be assigned. In summary, the perturbed C17-G18-A19 segment is consistent with the position of the DB[a,l]P residue on the 5′-side of G6*, the modified base.

Chemical Shifts. The chemical shift perturbations of the DNA nonexchangeable protons of the major conformer relative to its unmodified control duplex are depicted in Figure 4B. It was not possible to accurately assign some of the deoxyribose protons because of the significant distortion of the DNA structure caused by the DB[a,l]P residue. Nevertheless, some additional useful insights into the overall conformational features of this adduct can be gleaned from the changes in chemical shifts exhibited by the H1′, H2′, and H4′ deoxyribose protons and the H6/H8 base protons (Figure 4B). Upfield or downfield chemical shifts of sugar proton resonances can be observed from the T4 to C7 residues on the modified strand, and from the G16 to A19 residues on the complementary strand. Interesting differences are evident between the chemical shifts observed in the case of the 14S-DB[a,l]P-dG·Del (Figure 4A) and DB[a,l]P-dG full 11-mer duplexes (Figure 4B). For example, in the case of the Del duplex, the H2″ proton of C5 is upfield-shifted, while in the full duplex, it is downfield-shifted,
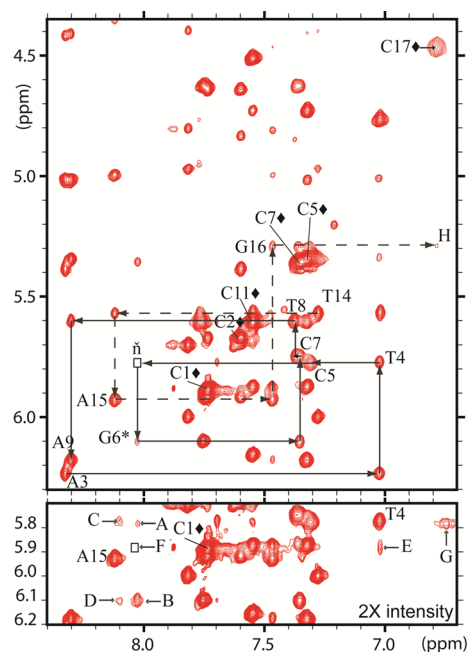
Figure 7. NMR characteristics of 11/11-mer duplexes in D$_2$O. Expanded contour plot of a NOESY spectrum (200 ms mixing time) recorded at 11 °C focused on the base (purine H8 and pyrimidine H6) and base (pyrimidine H5) and sugar H1′ proton region. The NOEs between the 2.45 Å fixed distance for the cytosine H5 to H6 are designated by diamonds. Sequential assignment for the segment formed by bases from A3 to A9 is indicated by the solid lines without disruption in the modified strand, although some cross-peaks are very weak (cross-peak A; see the bottom panel). For the nonmodified strand, the sequential assignment for the T14-A15-G16-C17-G18-A19-T20-G21-G22 segment (dashed lines) cannot be followed entirely. A disruption is observed from C17 to T20; elsewhere, the NOE connectivities can be traced without further interruption. The bottom panel shows a portion of the top panel contour plot level at 2× intensity revealing some weak cross-peaks labeled from A to G: (A) C5(H1′)−G6*(H8), (B) G6*(H8)−G6*(H1′), (C) T4(H1′)−DB-[a,l]P(H4), (D) G6*(H1′)−DB[a,l]P(H1), (E) T20(H8)−A19-(H1′), (F) A19(H8)−A19(H1′), and (G) C5(H1′)−DB[a,l]P(H3).

pointing to differences in the orientation of the DB[a,l]P aromatic ring systems in these different duplexes. In the case of the unmodified strand, the perturbations in chemical shifts occur mainly in the G16-G18 region; in the full duplex, the disturbance extends from the beginning to the end of the A15-G16-C17-G18-A19 segment. This is also consistent with an orientation of the DB[a,l]P ring system that is external to the helix and extends to base A19 of the unmodified strand. Taken together, the data suggest that the DB[a,l]P aromatic rings in the dominant conformation are located in the minor groove pointing toward the 5′-side of the lesion, although not in a classical minor groove conformation with all Watson−Crick base pairing maintained as in the case of the stereochemically analogous B[a]P-N^2-dG adduct in the same sequence context.[29,30]

NMR Assignment of the DB[a,l]P Proton Resonances. The nonexchangeable carcinogen protons were assigned from the analysis of through-bond TOCSY and through-space NOESY connectivities.[50] The chemical shifts at 11 °C of the aliphatic and aromatic DB[a,l]P ring protons are listed in Table 3 and graphically presented in Figure S5 of the Supporting Information.

Table 3. Observed Intermolecular NOEs in the 14S-DB[a,l]P-dG·C 11/11-mer Duplex and Achieved Distances from the Representative Structure in the Restrained MD Simulation[a]

DB[a,l]P proton	chemical shift (ppm)	NOE	intensity[a]	achieved distance (Å)
H1	8.1	G6*(H1′)	W	5.5
H2	6.7	C5(H5)	W	6.0
H3	6.7	C5(H1′)	W	5.7
		C5(H2′1)	M-W	6.0
		C5(H2′2)	W	4.3
H4	8.1	T4(H1′)	W	4.9
H5	8.4			
H6	7.7	C17(H5)	W	5.6
H7	7.8			
H8	7.8			
H9	8.4			
H10	7.6			
H11	4.0	G16(H1)	W	5.1
H12	5.1	G6*(H2′1)	W	6.0
		G6*(H2′2)	W	5.8
H13	4.3	G16(H1)	W	4.8
		C7(H2′2)	W	5.6
		G6*(H8)	W	6.1
		C7(H1′)	M	3.8
H14	6.5	G6*(H1′)	W	4.3
		C7(H1′)	W	6.0

[a]Experimentally observed NOEs were employed as restraint bounds in the distance-restrained MD simulation. The following bounds were assigned on the basis of the observed intensities: [M] = 3.5−4.5 Å, [W] = 4.5−6.0 Å, [M−W] = 3.5−6.0 Å. M for medium and W for weak.

Intermolecular NOEs. A total of 16 intermolecular NOEs were identified and assigned between the nonexchangeable DB[a,l]P protons and the exchangeable and nonexchangeable DNA protons. These intermolecular NOEs were classified as strong, medium, medium-weak, and weak according to the number of contour lines at the same threshold (Table 3). Most of the intermolecular NOEs observed involve protons on the DB[a,l]P residue and the modified DNA strand. The presence of the NOE between DB[a,l]P(H4) and T4(H1′) indicates that the DB[a,l]P aromatic ring system extends up to T4, which is also consistent with a minor groove location. The 5′-orientation of the DB[a,l]P aromatic ring system is further supported by the 2D imino proton spectrum in H$_2$O (Figure 6A), which clearly demonstrates that the G6*:C17 and C5:G18 base pairs are mainly disrupted, while the 1D spectra in Figure S6 of the Supporting Information indicate that the T4:A19 base pair is also destabilized. Consistent with this orientation, the aliphatic ring system protons of the DB[a,l]P residue exhibit NOEs with protons of the C7:G16 base pair (Table 1).

Distance-Restrained MD Model. Many of the structural details of the minor groove 14S-DB[a,l]P-dG adduct in the full duplex remain poorly defined because of overlapping and/or missing NOE connectivities, indicating significant conformational flexibility and/or broadening of some of the important resonances in the vicinity of the DB[a,l]P residue. However, the available DB[a,l]P residue−DNA connectivities yield a number of distance restraints that allowed for the modeling of this minor groove structure by MD simulation methods.

Distance-restrained MD simulations were conducted for a 5′-directed minor groove conformation utilizing the restraints

listed in Table 3. The initial model was created on the basis of the B[*a*]P-dG minor groove NMR solution structure[29] and subjected to restrained MD as detailed in Methods. Because of the conformational heterogeneity, weak NOEs, and unidentified cross-peaks, it was not possible to conduct intensity refinements.

The distance-refined model of the major conformation of the 14S-DB[*a,l*]P-dG adduct in the full duplex is shown in Figure 5C, while Table 3 shows that the achieved distances are within the range of the target values. While the bulky DB[*a,l*]P moiety with its five aromatic rings resides in the B-DNA minor groove and points toward the 5′-direction of the modified strand like the analogous B[*a*]P moiety, its accommodation in this groove is very different. Instead of fitting into the contours of the minor groove without excessive distortions, the DB[*a,l*]P ring system causes a marked enlargement and widening of the groove mainly on the 5′-side of G6* (Figures S8 and S9 of the Supporting Information); one face of the DB[*a,l*]P ring system is in close contact with the opened minor groove, with its large surface area achieving strong van der Waals interactions with the minor groove wall, while the other face is exposed to solvent (Figure S8 of the Supporting Information). The Watson−Crick hydrogen bond at the lesion-modified base pair (G6*:C17) and the 5′-flanking base pair (C5:G18) is ruptured, and the T4:A19 base pair is disrupted in 31% of the ensemble population (Table S5 of the Supporting Information). C17 stacks with the DB[*a,l*]P aromatic ring system, which is consistent with the upfield shift of the C17 protons. Furthermore, the duplex is also significantly unwound and untwisted at the G6*:C17 to C7:G16 adduct binding site, and this untwisting is compensated by overtwisting at the adjacent C7:G16 to T8:A15 step (Figure S9 of the Supporting Information).

■ DISCUSSION

The results of this study show that the size and shape of the aromatic ring system can give rise not only to pronounced differences in the conformations of the PAH diol epoxide DNA adducts formed but also to different extents of distortion of the surrounding DNA structure. Key features are the size of the aromatic ring system, its topology, the base sequence context, and the lesion stereochemistry. Here we compare the structure of the fjord 14S-DB[*a,l*]P-dG adduct with that of the topologically similar but smaller 1S-B[*c*]Ph-dG adduct, and that of the topologically different and configurationally identical 10S-B[*a*]P-dG adduct (Figure 1A). We also compare the structures of the 14S- and 14R-DB[*a,l*]P-dG adducts. Finally, we consider how the structural features of the lesions provide insights into their relative susceptibilities to excision by the human NER system.

Minor Groove and Intercalation Structures in Full Duplexes: Effects of PAH Adduct Topology. The stereochemically similar and planar four-ring bay region 10S-B[*a*]P-dG·dC adduct[29] (Figure S10 of the Supporting Information) shares features with the 14S-DB[*a,l*]P-dG·dC adduct in full 11/11-mer duplexes with identical sequence contexts. However, there are very significant differences due to the additional DB[*a,l*]P aromatic ring in the fjord region (Figure 1A). These two adducts share the same minor groove structures with the bulky aromatic ring systems being oriented on the 5′-side of the modified guanine residue (G6*). In each adduct, one face of the polycyclic aromatic ring system is exposed to the solvent while the other side is in van der Waals contact with the groove

walls. In the case of the B[*a*]P-dG adduct, all Watson−Crick base pairs are maintained in the full duplex and there is no evidence of any severe structural distortions of the duplex, although the minor groove is somewhat widened.[29] In the case of the DB[*a,l*]P-dG adduct, the wider aromatic ring system with the additional nonplanar aromatic ring in the fjord region causes a much greater opening of the minor groove, and the aromatic rings contact the minor groove face-on. By contrast, the aromatic ring system is inserted edge-on into the minor groove in the case of the B[*a*]P-dG·dC adduct (Figure S10 of the Supporting Information).[51,52] Moreover, C17, the partner base of G6*, stacks with the DB[*a,l*]P aromatic ring system as manifested by the upfield shift of the C17(H6) base proton. This stacking partly shields one face of the DB[*a,l*]P aromatic ring from the solvent (Figure 5C and Figure S8 of the Supporting Information).

In the case of the B[*a*]P-dG adduct, all of the base pairs, including the modified G6*:C17 base pair, are intact; however, in the case of the DB[*a,l*]P-dG adduct full duplex, the G18:C5 and G6*:C17 base pairs and, to a lesser extent, the T4:A19 pair are destabilized (Figure 5C). The destabilization of base pairs is supported by the absence of imino to amino cross-peaks between the C5:G18 and G6*:C17 base pairs. However, some evidence of episodic or weak hydrogen bonding is evident from the presence of weak and broadened imino proton resonances of G18 and G6* (Figure S6 of the Supporting Information). We speculate that conformational flexibility might allow the DB[*a,l*]P rings to infrequently assume a conformation more like that of the bay region B[*a*]P adduct with its aromatic ring edges pointing into the groove and all Watson−Crick base pairs maintained and distinguishable.

The much smaller three-ring fjord region 1S-B[*c*]Ph-dG adduct lacks the two 5,6,7,8,9 aromatic rings of the 14S-DB[*a,l*]P-dG adduct (Figure 1A), is smaller by one aromatic ring, and has an aromatic ring topology different from that of the bay region 10S-B[*a*]P-dG adduct. Because all three adducts have identical stereochemical properties, they offer the opportunity to evaluate the effects of other structural variables such as the topology and size of the aromatic ring systems on DNA adduct conformations and, ultimately, their biological responses.

In the case of the full duplexes with the identical sequence shown in Figure 1, only the 1S-B[*c*]Ph-dG·dC adduct assumes an intercalated conformation with the aromatic B[*c*]Ph residue inserted between the G18:C5 and G6*:C17 base pairs flanking the modified base pair on the 5′-side.[31] The Watson−Crick base pairing, though distorted, is maintained at the 1S-B[*c*]Ph-dG adduct site and beyond (Figure S10 of the Supporting Information).[31] The energetic considerations that come into play in determining whether a polycyclic aromatic ring system resides in a groove or is intercalated are multifaceted in nature: intercalation is favored by withdrawal of the aromatic rings from the aqueous solvent and stacking interactions with the DNA bases. The minor groove conformation in the case of the B[*a*]P-dG adduct has the advantage of retaining Watson−Crick pairing and normal base stacking interactions, with minimal distortions of the normal B-DNA structure.[51,52] However, the minor groove conformation of the 14S-DB[*a,l*]P-dG adduct has two or three destabilized base pairs, severe distortions in the minor groove dimensions, and significant solvent exposure of the large aromatic ring system. The question of why the 14S-DB[*a,l*]P-dG adduct adopts this unfavorable minor groove conformation rather than an intercalated one like that of the 1S-

B[*c*]Ph-dG adduct arises. A logical possibility is that the distorting penalty of intercalation is even greater than the distorting penalty of this minor groove structure. To examine this possibility, we created an intercalated model of the 14*S*-DB[*a,l*]P-dG adduct (Figure S11 of the Supporting Information) based on the 1*S*-B[*c*]Ph-dG NMR structure with intact Watson–Crick pairs[31] (Figure S10 of the Supporting Information) and compared these two structures. An analysis presented in the Supporting Information indicates that the intercalation structure would have destabilizing properties stemming from the positioning of the diol epoxide ring in the DNA minor groove that would disfavor intercalation.

Comparison of the 14*S*-DB[*a,l*]P-dG Deletion Duplex with the 10*S*-B[*a*]P-dG Deletion Duplex. Both the 14*S*-DB[*a,l*]P-dG and 10*S*-B[*a*]P-dG adducts adopt intercalated conformations in deletion duplexes. Although the partner nucleotide opposite the G6* adduct is absent, the backbone is stretched so that the adjacent Watson–Crick base pairs are maintained. The aromatic rings stack with the flanking C5:G18 and C7:G16 base pairs, while the benzylic rings with the attached guanine are positioned in the more wide and spacious major groove. However, the orientations of the adducts are different. In the 10*S*-B[*a*]P-dG·Del adduct (Figure S10 of the Supporting Information), the long axis of the B[*a*]P ring system is perpendicular to the long axis of the flanking base pairs; as a result, the benzylic ring is on the major groove side, the distal aromatic rings protrude into the minor groove, and the aromatic ring system is not in immediate contact with the unmodified partner strand. By contrast, in the DB[*a,l*]P adduct, the additional 1,2,3,4 DB[*a,l*]P ring is close to the modified strand and the aromatic ring system is shifted toward the partner strand (Figure 5A,B). With the DB[*a,l*]P aromatic ring system near the partner strand, the intercalation pocket is close to uniform in rise, while the pocket is wedge-shaped in the case of the polycyclic aromatic residue 10*S*-B[*a*]P-dG·Del adduct (Figure S10 of the Supporting Information). Factors that stabilize an intercalative rather than a minor groove conformation in the 14*S*-DB[*a,l*]P-dG deletion duplex are considered in the Supporting Information.

Comparison of 14*S*- and 14*R*-DB[*a,l*]P-dG Full Duplexes. While the 14*S*-DB[*a,l*]P-dG adduct in the full duplex is situated in the minor groove and is highly flexible and distorting, the 14*R*-DB[*a,l*]P-dG adduct adopts a stable conformation with intercalation from the narrow minor groove on the 3′-side of the damaged guanine. Hydrogen bonding with the partner cytosine is lost as the base pair is stretched due to the intercalation of the bulky ring system; this results in weakened stacking of the adjacent base pairs with the DB[*a,l*]P aromatic rings.[32] Severe opening of the major and minor grooves accompanies this stretching. This striking stereo-isomer-dependent structural difference is a manifestation of the "*S*" effect in PAH-derived stereoisomeric DNA adducts,[53] which characterizes the steric effects that cause greater conformational flexibility in adducts with *S* than with *R* stereochemistry at the linkage site. Other factors that may determine the minor groove versus intercalative positioning in the *S* versus *R* DB[*a,l*]P-dG stereoisomeric adducts are considered in the Supporting Information.

Relationship to Nucleotide Excision Repair. We have recently shown that the minor groove-positioned 14*S*-DB[*a,l*]P-dG adduct in double-stranded DNA is modestly repaired as compared to the well-repaired 14*R*-DB[*a,l*]P-dG adduct in HeLa cell extracts.[33] The NER efficiency of this 14*S*

adduct is similar to that of the 10*S*- and 10*R*-B[*a*]P-dG adducts,[28,33] which are positioned in minimally disturbed minor grooves pointing in the 5′- and 3′-directions relative to the modified guanines, respectively.[34] We attribute the smaller NER activity of the 14*S*-DB[*a,l*]P-dG adduct relative to that of the 14*R*-DB[*a,l*]P-dG adduct to the extensive van der Waals interactions between the DB[*a,l*]P aromatic rings and DNA residues in the minor groove, as well as to the stacking interactions of the DB[*a,l*]P aromatic ring system with the C17 base in the 14*S* case (Figure 5C). On the other hand, the intercalative insertion of the large DB[*a,l*]P aromatic ring on the 3′-side of G6* in the 14*R*-DB[*a,l*]P-dG adduct and the protrusion of the bulky benzylic ring into the crowded minor groove[32] disrupt the hydrogen bonding of the modified G6*:C17 base pair, cause a local widening of the major and minor grooves, and diminish the level of stacking between the DB[*a,l*]P aromatic rings and adjacent base pairs. Thus, the 14*R* adduct is more significantly destabilized than the minor groove 14*S*-DB[*a,l*]P-dG adduct whose distortions are partly compensated by the strong van der Waals interactions. The greater instability in the 14*R* case, manifested also in thermal melting data, is correlated with a higher NER activity of the 14*R* adduct versus that of the 14*S* adduct.[33]

The crystal structure of Rad4/Rad23, the yeast homologue of the human NER recognition factor XPC-RAD23B with a DNA duplex containing a thymine dimer lesion, shows that two bases opposite the lesion are flipped out of the helix and are bound to the protein, while its BHD3 *β*-hairpin is inserted between the two DNA strands.[54] We have hypothesized that the van der Waals interactions between the adducts and local DNA residues could inhibit the productive hairpin intrusion.[55] Thus the recognition step and the ease of local separation of the two strands in the vicinity of the DNA lesion play a role in the NER activity. In turn, the ease of strand separation associated with the presence of an adducted base would be related to the extent of local thermodynamic destabilization of the DNA duplex,[54,56] which is determined by the balance between destabilizing and stabilizing interactions produced by the adduct.[53]

■ ASSOCIATED CONTENT

ⓢ Supporting Information

Experimental NMR TOCSY and NOSEY spectra and nucleic acid chemical shifts of the 14*S*-DB[*a,l*]P-dG deletion duplex, 1D spectra at different temperatures (full duplex), an experimental NMR NOSEY spectrum and nucleic acid chemical shifts of the full duplex, comparison of chemical shifts of DB[*a,l*]P protons in deletion and full duplexes, details of the MD simulation protocol and force field parameters of the 14*S*-DB[*a,l*]P-dG full duplex, superposition of five representative structures of the 14*S*-DB[*a,l*]P-dG deletion duplex, the central 4-mer of the full duplex in CPK, twist and minor groove widths, an intercalated model for the 14*S*-DB[*a,l*]P-dG full duplex, further discussion concerning factors governing conformational selection in DB[*a,l*]P adducts, and structures of 10*S*-B[*a*]P-dG·Del, 10*S*-B[*a*]P-dG·dC, and 1*S*-B[*c*]Ph-dG·dC in full duplexes. This material is available free of charge via the Internet at http://pubs.acs.org.

Accession Codes

NMR structures of the 14*S*-DB[*a,l*]P-dG adduct in deletion and full duplexes have been deposited as Protein Data Bank entries 2MIV and 2MIW, respectively.

■ AUTHOR INFORMATION

Corresponding Author

*E-mail: ng1@nyu.edu. Phone: (212) 998-8407. Fax: (212) 998-8421.

Notes

The authors declare no competing financial interest.

■ ABBREVIATIONS

PAHs, polycyclic aromatic hydrocarbons; DB[a,l]P, dibenzo-[a,l]pyrene; B[c]Ph, benzo[c]phenanthrene; B[a]P, benzo[a]-pyrene; 14S-DB[a,l]P-dG, 14S-(−)-trans-anti-DB[a,l]P-N^2-dG; 10S-B[a]P-dG, 10S-(+)-trans-anti-B[a]P-N^2-dG; 14S-B[c]Ph-dG, 14S-(−)-trans-anti-B[c]Ph-N^2-dG; MD, molecular dynamics; NER, nucleotide excision repair; rmsd, root-mean-square deviation; NOESY, nuclear Overhauser effect spectroscopy; COSY, correlated spectroscopy; TOCSY, total COSY; 2D, two-dimensional.

■ REFERENCES

(1) Bostrom, C. E., Gerde, P., Hanberg, A., Jernstrom, B., Johansson, C., Kyrklund, T., Rannug, A., Tornqvist, M., Victorin, K., and Westerholm, R. (2002) Cancer risk assessment, indicators, and guidelines for polycyclic aromatic hydrocarbons in the ambient air. *Environ. Health Perspect. 110* (Suppl. 3), 451−488.

(2) Pfeifer, G. P., Denissenko, M. F., Olivier, M., Tretyakova, N., Hecht, S. S., and Hainaut, P. (2002) Tobacco smoke carcinogens, DNA damage and p53 mutations in smoking-associated cancers. *Oncogene 21*, 7435−7451.

(3) Chakravarti, D., Venugopal, D., Mailander, P. C., Meza, J. L., Higginbotham, S., Cavalieri, E. L., and Rogan, E. G. (2008) The role of polycyclic aromatic hydrocarbon-DNA adducts in inducing mutations in mouse skin. *Mutat. Res. 649*, 161−178.

(4) Penning, T. M. (2010) Polycyclic aromatic hydrocarbons: Multiple metabolic pathways and the DNA lesions formed. In *The Chemical Biology of DNA Damage* (Geacintov, N. E., and Broyde, S., Eds.) pp 131−155, Wiley-VCH Verlag GmbH & Co. KGaA, Weinheim, Germany.

(5) Cheng, S. C., Hilton, B. D., Roman, J. M., and Dipple, A. (1989) DNA adducts from carcinogenic and noncarcinogenic enantiomers of benzo[a]pyrene dihydrodiol epoxide. *Chem. Res. Toxicol. 2*, 334−340.

(6) Li, K. M., George, M., Gross, M. L., Lin, C. H., Jankowiak, R., Small, G. J., Seidel, A., Kroth, H., Rogan, E. G., and Cavalieri, E. L. (1999) Structure elucidation of the adducts formed by fjord region dibenzo[a,l]pyrene-11,12-dihydrodiol 13,14-epoxides with deoxyguanosine. *Chem. Res. Toxicol. 12*, 778−788.

(7) Conney, A. H. (1982) Induction of microsomal enzymes by foreign chemicals and carcinogenesis by polycyclic aromatic hydrocarbons: G. H. A. Clowes Memorial Lecture. *Cancer Res. 42*, 4875−4917.

(8) Lehr, R. E., and Jerina, D. M. (1977) Metabolic activations of polycyclic hydrocarbons. Structure-activity relationships. *Arch. Toxicol. 39*, 1−6.

(9) Li, K. M., Byun, J., Gross, M. L., Zamzow, D., Jankowiak, R., Rogan, E. G., and Cavalieri, E. L. (1999) Synthesis and structure determination of the adducts formed by electrochemical oxidation of dibenzo[a,l]pyrene in the presence of adenine. *Chem. Res. Toxicol. 12*, 749−757.

(10) Koreeda, M., Moore, P. D., Wislocki, P. G., Levin, W., Yagi, H., and Jerina, D. M. (1978) Binding of benzo[a]pyrene 7,8-diol-9,10-epoxides to DNA, RNA, and protein of mouse skin occurs with high stereoselectivity. *Science 199*, 778−781.

(11) Weinstein, I. B., Jeffrey, A. M., Jennette, K. W., Blobstein, S. H., Harvey, R. G., Harris, C., Autrup, H., Kasai, H., and Nakanishi, K. (1976) Benzo(a)pyrene diol epoxides as intermediates in nucleic acid binding in vitro and in vivo. *Science 193*, 592−595.

(12) Dreij, K., Seidel, A., and Jernstrom, B. (2005) Differential removal of DNA adducts derived from anti-diol epoxides of dibenzo[a,l]pyrene and benzo[a]pyrene in human cells. *Chem. Res. Toxicol. 18*, 655−664.

(13) Ralston, S. L., Seidel, A., Luch, A., Platt, K. L., and Baird, W. M. (1995) Stereoselective activation of dibenzo[a,l]pyrene to (−)-anti(11R,12S,13S,14R)- and (+)-syn(11S,12R,13S,14R)-11,12-diol-13,14-epoxides which bind extensively to deoxyadenosine residues of DNA in the human mammary carcinoma cell line MCF-7. *Carcinogenesis 16*, 2899−2907.

(14) Spencer, W. A., Singh, J., and Orren, D. K. (2009) Formation and differential repair of covalent DNA adducts generated by treatment of human cells with (±)-anti-dibenzo[a,l]pyrene-11,12-diol-13,14-epoxide. *Chem. Res. Toxicol. 22*, 81−89.

(15) Lagerqvist, A., Hakansson, D., Prochazka, G., Lundin, C., Dreij, K., Segerback, D., Jernstrom, B., Tornqvist, M., Seidel, A., Erixon, K., and Jenssen, D. (2008) Both replication bypass fidelity and repair efficiency influence the yield of mutations per target dose in intact mammalian cells induced by benzo[a]pyrene-diol-epoxide and dibenzo[a,l]pyrene-diol-epoxide. *DNA Repair 7*, 1202−1212.

(16) Prahalad, A. K., Ross, J. A., Nelson, G. B., Roop, B. C., King, L. C., Nesnow, S., and Mass, M. J. (1997) Dibenzo[a,l]pyrene-induced DNA adduction, tumorigenicity, and Ki-ras oncogene mutations in strain A/J mouse lung. *Carcinogenesis 18*, 1955−1963.

(17) Amin, S., Desai, D., Dai, W., Harvey, R. G., and Hecht, S. S. (1995) Tumorigenicity in newborn mice of fjord region and other sterically hindered diol epoxides of benzo[g]chrysene, dibenzo[a,l]-pyrene (dibenzo[def,p]chrysene), 4H-cyclopenta[def]chrysene and fluoranthene. *Carcinogenesis 16*, 2813−2817.

(18) Hecht, S. S., el-Bayoumy, K., Rivenson, A., and Amin, S. (1994) Potent mammary carcinogenicity in female CD rats of a fjord region diol-epoxide of benzo[c]phenanthrene compared to a bay region diol-epoxide of benzo[a]pyrene. *Cancer Res. 54*, 21−24.

(19) Luch, A. (2009) On the impact of the molecule structure in chemical carcinogenesis. *EXS 99*, 151−179.

(20) Luch, A. (2005) Nature and nurture: Lessons from chemical carcinogenesis. *Nat. Rev. Cancer 5*, 113−125.

(21) Cavalieri, E. L., Higginbotham, S., RamaKrishna, N. V., Devanesan, P. D., Todorovic, R., Rogan, E. G., and Salmasi, S. (1991) Comparative dose-response tumorigenicity studies of dibenzo-[a,l]pyrene versus 7,12-dimethylbenz[a]anthracene, benzo[a]pyrene and two dibenzo[a,l]pyrene dihydrodiols in mouse skin and rat mammary gland. *Carcinogenesis 12*, 1939−1944.

(22) Cavalieri, E. L., Higginbotham, S., and Rogan, E. G. (1994) Dibenzo[a,I]pyrene: The most potent carcinogenic aromatic hydro-carbon. *Polycyclic Aromat. Compd. 6*, 177−183.

(23) Guttenplan, J. B., Kosinska, W., Zhao, Z. L., Chen, K. M., Aliaga, C., Deltondo, J., Cooper, T., Sun, Y. W., Zhang, S. M., Jiang, K., Bruggeman, R., Sharma, A. K., Amin, S., Ahn, K., and El-Bayoumy, K. (2011) Mutagenesis and carcinogenesis induced by dibenzo[a,l]pyrene in the mouse oral cavity: A potential new model for oral cancer. *Int. J. Cancer 130*, 2783−2790.

(24) Yoon, J. H., Besaratinia, A., Feng, Z., Tang, M. S., Amin, S., Luch, A., and Pfeifer, G. P. (2004) DNA damage, repair, and mutation induction by (+)-*syn* and (-)-*anti*-dibenzo[a,l]pyrene-11,12-diol-13,14-epoxides in mouse cells. *Cancer Res. 64*, 7321−7328.

(25) Zhang, S. M., Chen, K. M., Aliaga, C., Sun, Y. W., Lin, J. M., Sharma, A. K., Amin, S., and El-Bayoumy, K. (2011) Identification and quantification of DNA adducts in the oral tissues of mice treated with the environmental carcinogen dibenzo[a,l]pyrene by HPLC-MS/MS. *Chem. Res. Toxicol. 24*, 1297−1303.

(26) Buterin, T., Hess, M. T., Luneva, N., Geacintov, N. E., Amin, S., Kroth, H., Seidel, A., and Naegeli, H. (2000) Unrepaired fjord region polycyclic aromatic hydrocarbon-DNA adducts in ras codon 61 mutational hot spots. *Cancer Res. 60*, 1849−1856.

(27) Kropachev, K., Kolbanovskiy, M., Rodriguez, F. A., Cai, Y. Q., Ding, S., Zhang, L., Amin, S., Broyde, S., and Geacintov, N. E. (2010) Dibenzo[a,l]pyrene Diol Epoxide-adenine but Not -Guanine Adducts Are Resistant to Nucleotide Excision Repair in Human Cell Extracts. *Chem. Res. Toxicol. 23*, 282−282.

(28) Hess, M. T., Gunz, D., Luneva, N., Geacintov, N. E., and Naegeli, H. (1997) Base pair conformation-dependent excision of benzo[a]pyrene diol epoxide-guanine adducts by human nucleotide excision repair enzymes. *Mol. Cell. Biol. 17*, 7069−7076.

(29) Cosman, M., de los Santos, C., Fiala, R., Hingerty, B. E., Singh, S. B., Ibanez, V., Margulis, L. A., Live, D., Geacintov, N. E., Broyde, S., et al. (1992) Solution conformation of the major adduct between the carcinogen (+)-*anti*-benzo[a]pyrene diol epoxide and DNA. *Proc. Natl. Acad. Sci. U.S.A. 89*, 1914−1918.

(30) Cosman, M., Fiala, R., Hingerty, B. E., Amin, S., Geacintov, N. E., Broyde, S., and Patel, D. J. (1994) Solution conformation of the (+)-*trans-anti*-[BP]dG adduct opposite a deletion site in a DNA duplex: Intercalation of the covalently attached benzo[a]pyrene into the helix with base displacement of the modified deoxyguanosine into the major groove. *Biochemistry 33*, 11507−11517.

(31) Lin, C. H., Huang, X., Kolbanovskii, A., Hingerty, B. E., Amin, S., Broyde, S., Geacintov, N. E., and Patel, D. J. (2001) Molecular topology of polycyclic aromatic carcinogens determines DNA adduct conformation: A link to tumorigenic activity. *J. Mol. Biol. 306*, 1059−1080.

(32) Tang, Y., Liu, Z., Ding, S., Lin, C. H., Cai, Y., Rodriguez, F. A., Sayer, J. M., Jerina, D. M., Amin, S., Broyde, S., and Geacintov, N. E. (2012) Nuclear magnetic resonance solution structure of an N²-guanine DNA adduct derived from the potent tumorigen dibenzo-[a,l]pyrene: Intercalation from the minor groove with ruptured Watson-Crick base pairing. *Biochemistry 51*, 9751−9762.

(33) Kropachev, K., Kolbanovskiy, M., Liu, Z., Cai, Y., Zhang, L., Schwaid, A. G., Kolbanovskiy, A., Ding, S., Amin, S., Broyde, S., and Geacintov, N. E. (2013) Adenine-DNA Adducts Derived from the Highly Tumorigenic Dibenzo[a,l]pyrene Are Resistant to Nucleotide Excision Repair while Guanine Adducts Are Not. *Chem. Res. Toxicol. 26*, 783−793.

(34) de los Santos, C., Cosman, M., Hingerty, B. E., Ibanez, V., Margulis, L. A., Geacintov, N. E., Broyde, S., and Patel, D. J. (1992) Influence of benzo[a]pyrene diol epoxide chirality on solution conformations of DNA covalent adducts: The (-)-*trans-anti*-[BP]G·

C adduct structure and comparison with the (+)-*trans-anti*-[BP]G·C enantiomer. *Biochemistry 31*, 5245−5252.

(35) Wang, B., Sayer, J. M., Yagi, H., Frank, H., Seidel, A., and Jerina, D. M. (2006) Facile interstrand migration of the hydrocarbon moiety of a dibenzo[a,l]pyrene 11,12-diol 13,14-epoxide adduct at N² of deoxyguanosine in a duplex oligonucleotide. *J. Am. Chem. Soc. 128*, 10079−10084.

(36) Goddard, T. D., and Kneller, D. G. (2006) *SPARKY 3*, University of California, San Francisco.

(37) Frisch, M. J., Trucks, G. W., Schlegel, H. B., Scuseria, G. E., Robb, M. A., Cheeseman, J. R., Montgomery, J. A., Jr., Vreven, T., Kudin, K. N., Burant, J. C., Millam, J. M., Iyengar, S. S., Tomasi, J., Barone, V., Mennucci, B., Cossi, M., Scalmani, G., Rega, N., Petersson, G. A., Nakatsuji, H., Hada, M., Ehara, M., Toyota, K., Fukuda, R., Hasegawa, J., Ishida, M., Nakajima, T., Honda, Y., Kitao, O., Nakai, H., Klene, M., Li, X., Knox, J. E., Hratchian, H. P., Cross, J. B., Bakken, V., Adamo, C., Jaramillo, J., Gomperts, R., Stratmann, R. E., Yazyev, O., Austin, A. J., Cammi, R., Pomelli, C., Ochterski, J. W., Ayala, P. Y., Morokuma, K., Voth, G. A., Salvador, P., Dannenberg, J. J., Zakrzewski, V. G., Dapprich, S., Daniels, A. D., Strain, M. C., Farkas, O., Malick, D. K., Rabuck, A. D., Raghavachari, K., Foresman, J. B., Ortiz, J. V., Cui, Q., Baboul, A. G., Clifford, S., Cioslowski, J., Stefanov, B. B., Liu, G., Liashenko, A., Piskorz, P., Komaromi, I., Martin, R. L., Fox, D. J., Keith, T., Al-Laham, M. A., Peng, C. Y., Nanayakkara, A., Challacombe, M., Gill, P. M. W., Johnson, B., Chen, W., Wong, M. W., Gonzalez, C., and Pople, J. A. (2004) *Gaussian 03*, revision C.02, Gaussian, Inc., Wallingford, CT.

(38) Case, D. A., Darden, T. A., Cheatham, T. E., III, Simmerling, C. L., Wang, J., Duke, R. E., Luo, R., Merz, K. M., Wang, B., Pearlman, D. A., Crowley, M., Walker, R. C., Zhang, W., Wang, B., Hayik, S., Roitberg, A., Seabra, G., Wong, K. F., Paesani, F., Wu, X., Brozell, S., Tsui, V., Gohlke, H., Yang, L., Tan, C., Mongan, J., Hornak, V., Cui, G., Beroza, P., Mathews, D. H., Schafmeister, C., Ross, W. S., and Kollman, P. A. (2006) *AMBER 9*, University of California, San Francisco.

(39) Cieplak, P., Cornell, W. D., Bayly, C., and Kollman, P. A. (1995) Application of the Multimolecule and Multiconformational Resp Methodology to Biopolymers: Charge Derivation for DNA, RNA, and Proteins. *J. Comput. Chem. 16*, 1357−1377.

(40) Cheatham, T. E., Cieplak, P., and Kollman, P. A. (1999) A modified version of the Cornell et al. force field with improved sugar pucker phases and helical repeat. *J. Biomol. Struct. Dyn. 16*, 845−862.

(41) Bayly, C. I., Cieplak, P., Cornell, W. D., and Kollman, P. A. (1993) A Well-Behaved Electrostatic Potential Based Method Using Charge Restraints for Deriving Atomic Charges: The Resp Model. *J. Phys. Chem. 97*, 10269−10280.

(42) Borgias, B. A., and James, T. L. (1989) Two-dimensional nuclear Overhauser effect: Complete relaxation matrix analysis. *Methods Enzymol. 176*, 169−183.

(43) Patel, D. J., Shapiro, L., and Hare, D. (1987) DNA and RNA: NMR studies of conformations and dynamics in solution. *Q. Rev. Biophys. 20*, 35−112.

(44) Van de Ven, F. J., and Hilbers, C. W. (1988) Nucleic acids and nuclear magnetic resonance. *Eur. J. Biochem. 178*, 1−38.

(45) Gomes, J. A., and Mallion, R. B. (2001) Aromaticity and ring currents. *Chem. Rev. 101*, 1349−1383.

(46) Patel, D. J., Shapiro, L., and Hare, D. (1987) Nuclear magnetic resonance and distance geometry studies of DNA structures in solution. *Annu. Rev. Biophys. Biophys. Chem. 16*, 423−454.

(47) Altona, C., and Sundaral, M. (1972) Conformational-Analysis of Sugar Ring in Nucleosides and Nucleotides: New Description Using Concept of Pseudorotation. *J. Am. Chem. Soc. 94*, 8205−8212.

(48) Saenger, W. (1984) *Principles of Nucleic Acid Structure*, Springer-Verlag, New York.

(49) Patel, D. J., Kozlowski, S. A., Nordheim, A., and Rich, A. (1982) Right-Handed and Left-Handed DNA: Studies of B-DNA and Z-DNA by Using Proton Nuclear Overhauser Effect and P NMR. *Proc. Natl. Acad. Sci. U.S.A. 79*, 1413−1417.

(50) Rodriguez, F. (2007) Nuclear Magnetic Resonance Solution Structure of Covalent Polycyclic Aromatic Carcinogen−DNA Adducts: Influence of Base Sequence Contexts and Carcinogen Topology. Chemistry Department, New York University, New York.

(51) Yan, S., Wu, M., Patel, D. J., Geacintov, N. E., and Broyde, S. (2003) Simulating structural and thermodynamic properties of carcinogen-damaged DNA. *Biophys. J. 84*, 2137−2148.

(52) Mocquet, V., Kropachev, K., Kolbanovskiy, M., Kolbanovskiy, A., Tapias, A., Cai, Y., Broyde, S., Geacintov, N. E., and Egly, J. M. (2007) The human DNA repair factor XPC-HR23B distinguishes stereoisomeric benzo[*a*]pyrenyl-DNA lesions. *EMBO J. 26*, 2923− 2932.

(53) Cai, Y., Geacintov, N. E., and Broyde, S. (2012) Nucleotide excision repair efficiencies of bulky carcinogen-DNA adducts are governed by a balance between stabilizing and destabilizing interactions. *Biochemistry 51*, 1486−1499.

(54) Min, J. H., and Pavletich, N. P. (2007) Recognition of DNA damage by the Rad4 nucleotide excision repair protein. *Nature 449*, 570−575.

(55) Reeves, D. A., Mu, H., Kropachev, K., Cai, Y., Ding, S., Kolbanovskiy, A., Kolbanovskiy, M., Chen, Y., Krzeminski, J., Amin, S., Patel, D. J., Broyde, S., and Geacintov, N. E. (2011) Resistance of bulky DNA lesions to nucleotide excision repair can result from extensive aromatic lesion-base stacking interactions. *Nucleic Acids Res. 39*, 8752−8764.

(56) Scharer, O. D. (2008) A molecular basis for damage recognition in eukaryotic nucleotide excision repair. *ChemBioChem 9*, 21−23.

(57) Geacintov, N. E., Cosman, M., Hingerty, B. E., Amin, S., Broyde, S., and Patel, D. J. (1997) NMR solution structures of stereoisometric covalent polycyclic aromatic carcinogen-DNA adduct: Principles, patterns, and diversity. *Chem. Res. Toxicol. 10*, 111−146.